CRYSTAL GROWTH & DESIGN

Article

pubs.acs.org/crystal

Interplay of Noncovalent Interactions in Ribbon-like Guanosine Self-Assembly: An NMR Crystallography Study

G. N. Manjunatha Reddy,[§] Andrew Marsh,[†] Jeffery T. Davis,[‡] Stefano Masiero,[#] and Steven P. Brown*[,§]

[§]Department of Physics and [†]Department of Chemistry, University of Warwick, Coventry CV4 7AL, United Kingdom

[‡]Department of Chemistry and Biochemistry, University of Maryland, College Park, Maryland 20742, United States

[#]Dipartimento di Chimica "Giacomo Ciamician", Alma Mater Studiorum − Università di Bologna, 40126 Bologna, Italy

Supporting Information

ABSTRACT: An NMR crystallography study shows how intermolecular N−H···O, N−H···N, O−H···N, O−H···O, and CH−π interactions stabilize the ribbon-like supramolecular structures of three different guanosine derivatives: guanosine dihydrate (**G**), 3′,5′-*O*-dipropanolyl deoxyguanosine (**dG(C3)$_2$**), and 3′,5′-*O*-isopropylideneguanosine hemihydrate (**Gace**). Experimental solid-state ^{1}H NMR spectra obtained at 20 T using fast magic-angle spinning (MAS), here at 75 kHz, are presented for a dihydrate of **G**. For each guanosine derivative, the role of specific interactions is probed by means of NMR chemical shifts calculated using the density functional theory (DFT) gauge-including projector-augmented wave (GIPAW) approach for the full crystal and extracted isolated single molecules. Specifically, the isolated molecule to full crystal transformations result in net changes in the GIPAW calculated ^{1}H NMR chemical shifts of up to 8 ppm for O−H···O, up to 6.5 ppm for N−H···N and up to 4.6 ppm for N−H···O hydrogen bonds; notably, the presence of water molecules in **G** and **Gace** reinforces the molecular stacking through strong O−H···O hydrogen bonds. The sugar conformations are markedly different in **G**, **dG(C3)$_2$**, and **Gace**, and it is shown that the experimental ^{13}C solid-state NMR chemical shift at the C8 position is a reliable indicator of a "*syn*" (>135 ppm) or "*anti*" (<135 ppm) conformer.

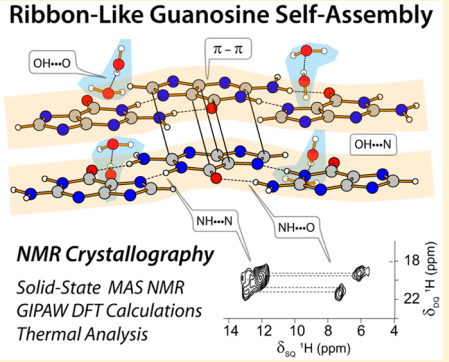

INTRODUCTION

Molecular self-assembly can be exploited to engineer biomimetic and functional materials in aqueous and organic solutions, on surfaces and in the solid state.[1−4] Characterization of noncovalent interactions such as hydrogen bonding and CH−π interactions at the molecular level is crucial to better understand the delicate balance between the forces that hold together supramolecular structure, to establish structure−property relationships and to improve their design and function.

Modified DNA/RNA bases, specifically guanosine (**G**, **1**) derivatives have the versatility to self-assemble into cyclic quartets, continuous helices and ribbon-like structures, as previously characterized by NMR, circular dichroism (CD), and X-ray data.[5−23] Whether the guanosine self-assembly is quartet/helical or ribbon-like, the intermolecular N−H···N and N−H···O hydrogen-bonding interactions play an important role, while several other molecular interactions such as electrostatic, π−π, CH−π, Coulombic interactions, van der Waals forces, and cation and anion binding also contribute to stabilizing the overall three-dimensional architectures. Such intermolecular interactions, notably, hydrogen bonding and aromatic ring current effects, have a dramatic effect on NMR chemical shifts.[24−33] By employing an NMR crystallography approach[34−36] using experimental solid-state NMR and GIPAW DFT calculations performed on the full crystal and extracted isolated molecules, we here investigate the role of noncovalent interactions driving the ribbon-like self-assembly in three guanosine derivatives: guanosine dihydrate **G**, 3′,5′-*O*-dipropanolyl deoxyguanosine **dG(C3)$_2$**, and 3′,5′-*O*-isopropylideneguanosine hemihydrate **Gace**. These guanine derivatives are functionally diverse; for example, lipophilic derivatives of **dG(C3)$_2$** and **Gace** substituted with longer alkyl chains are well-known to form lyotropic mesophases in organic solvents,[37] and once deposited on surfaces, these molecules exhibit photoconductive[38] and rectifying properties[39] and have potential applications in molecular electronics.[40,41]

RESULTS AND DISCUSSION

Crystal Packing and Intermolecular Interactions. Together with the chemical structures and atomic numbering, Figure 1 presents an overview of molecular packing in the guanosine derivatives **G**, **dG(C3)$_2$**, and **Gace**. Note that in each case, there are two crystallographically independent molecules in the asymmetric unit cell (Z' = 2), denoted here A and B. For **G**, the **G**-ribbons are composed of either purely type A molecules (−A···A···A−) or purely type B molecules (−B···B···B−), alternatingly stacked on top of each other. By comparison, ribbons of **dG(C3)$_2$** and **Gace** are composed of both type A

Received: October 8, 2015
Published: November 4, 2015

DOI: 10.1021/acs.cgd.5b01440
Cryst. Growth Des. 2015, 15, 5945−5954

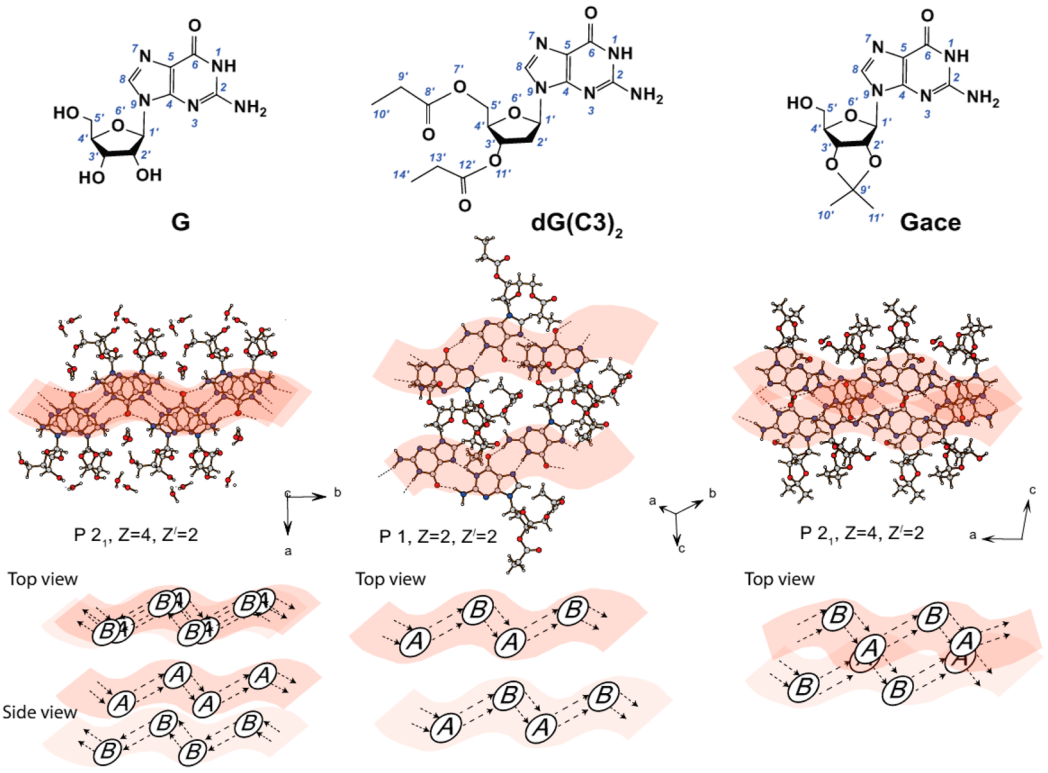

Figure 1. Molecular structures (top) along with atomic numbering of **G**, **dG(C3)$_2$**, and **Gace**. Overview of molecular packing in the ribbon-like guanosine self-assembly as driven by intermolecular NH···N and NH···O hydrogen bonds (middle). The crystallographic symmetry as well as the number of molecules in the unit cell (Z) and in the asymmetric unit cell (Z′) are stated. Cartoon representation of the ribbon-like structures (bottom) depicting the arrangement of the two crystallographically independent molecules, A and B. → represents the directionality of the hydrogen bonding interactions with the arrow pointing toward an acceptor site.

and type B molecules self-organized in the form of (−A···B···A−) with a loose stacking arrangement. The ribbon-like structures presented in Figure 1 are dipolar with the dipoles modulating along the axis of ribbon. Particularly in **dG(C3)$_2$**, the minimal inter-ribbon stacking is due to the substitution by short alkyl chains at the 2′ and 5′ positions causing steric hindrance between successive G-ribbons. Studies also reported that similar steric effects lead to a minimal base-stacking in other guanosine derivatives substituted with triisopropylsilyl and *t*-butylsilyl groups.[42,43]

Guanosine and its derivatives are known to be hygroscopic.[44,45] For **G**, a humidity-induced crystal transition occurs between hydrous and anhydrous forms passing through an intermediate meta-state.[46,47] The thermal analysis presented in Figure 2 reveals a 12.5% weight loss in **G**, which corresponds to a dihydrate form G·2H$_2$O. The crystal structure of the dihydrate form of **G** contains two types of water molecules, namely, interlayer water molecules (interconnecting sugar moieties in neighboring ribbon-like structures) and intralayer water molecules (intercalating between guanine frames of the **G**-ribbons).[47] As previously reported in ref 23, Figure 2 also shows that there is a 2.25% weight loss in **Gace** that corresponds to a hemihydrate form, **Gace·0.5H$_2$O**.

In this paper, the intermolecular hydrogen bonding interactions observed for the G-ribbon crystal structures are classified into (I) sharing donor−acceptor atoms between homologous molecules (A···A or B···B); (II) sharing donor−acceptor atoms between analogous molecules (A···B or B···A); (III) sharing donor−acceptor atoms between nucleobase and water molecules (A···W, B···W). Type (I) interactions are

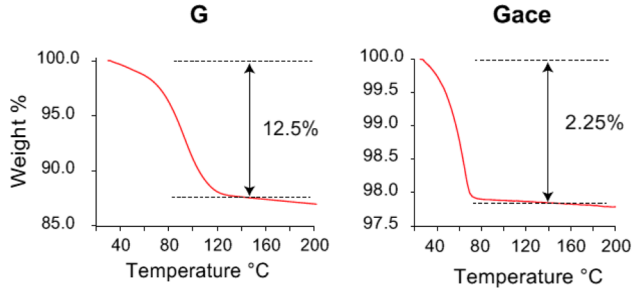

Figure 2. Themal analysis of **G** (left-hand side) showed a 12.5% weight loss which corresponds to a dihydrate form, **G·2H$_2$O**, while for **Gace** (right-hand side, data repeated from Figure 2 of ref 23), a 2.25% weight loss was observed, corresponding to the hemidihydrate form, **Gace·0.5H$_2$O**.

observed in **G** leading to the ribbon-like structures stacked antiparallel to each other; i.e., the directionality of G-ribbons containing molecules of type A is along the crystallographic axis *b*, while ribbons made up of type B molecules have an opposite directionality, along the axis −*b* (Figure 1). Type (II) interactions are observed in **dG(C3)$_2$** and **Gace**, where the ribbons are modulating parallel to each other. Type (III) interactions reinforce the three-dimensional stacking of ribbons whether they are stacked in a parallel (**Gace**) or in an antiparallel (**G**) manner.

Probing Ribbon-like Guanosine Self-Assembly in G by Solid-State NMR Spectroscopy and GIPAW DFT Calculations. In previous studies, solid-state MAS NMR spectroscopy has been used to identify the mode of self-assembly of

DOI: 10.1021/acs.cgd.5b01440
Cryst. Growth Des. 2015, 15, 5945−5954

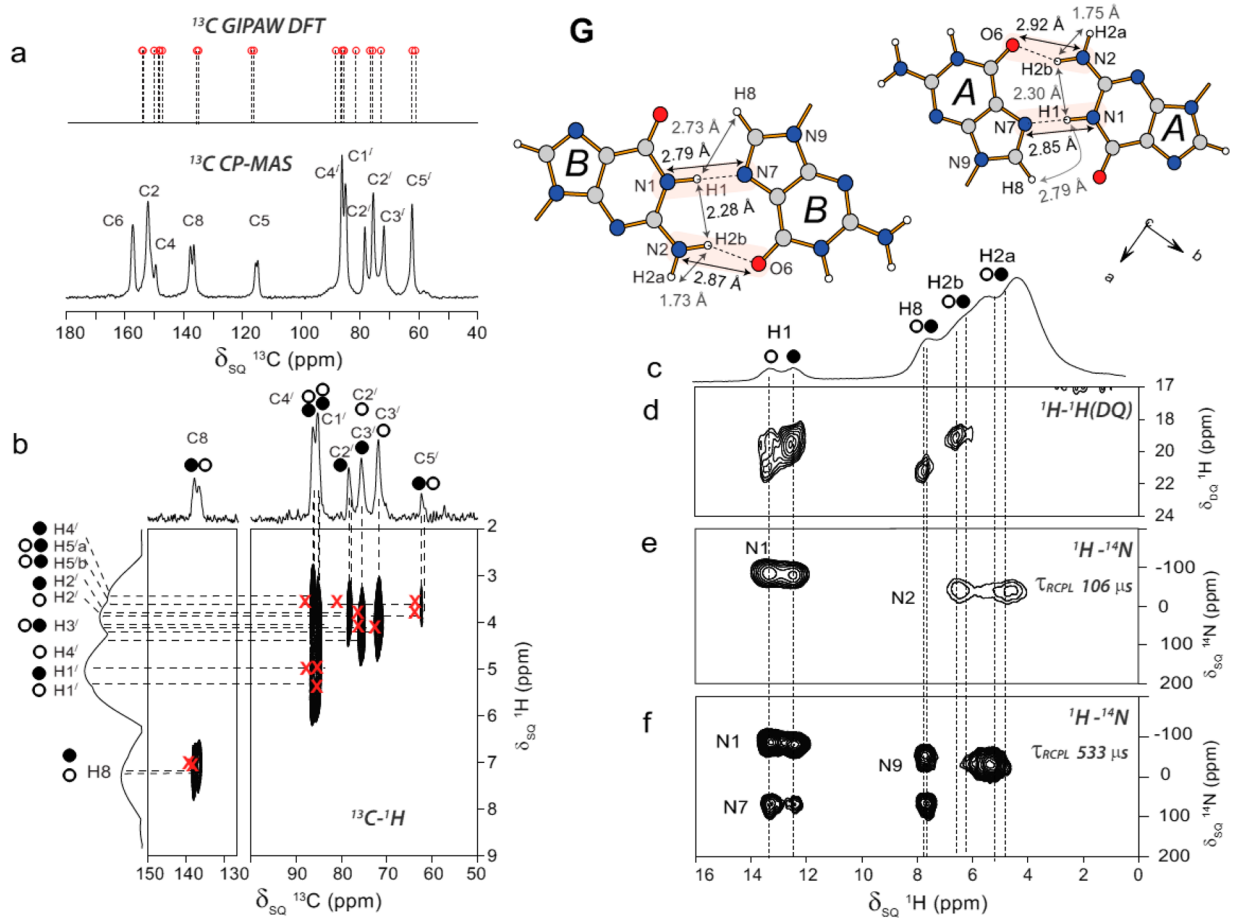

Figure 3. Experimental one- and two-dimensional solid-state MAS NMR spectra are presented together with GIPAW DFT NMR shielding calculations (see Table S1 in the Supporting Information) for **G** (filled and hollow circles correspond to the A and B molecules in the asymmetric unit cell, respectively). Left panel: (a) A stick spectrum of GIPAW calculated ^{13}C NMR chemical shifts is plotted on top of an experimental ^{13}C CP MAS spectrum (^{1}H 500 MHz, 10.0 kHz MAS), (b) a ^{13}C−^{1}H refocused INEPT spectrum (^{1}H 600 MHz, 12.5 kHz MAS using eDUMBO-1$_{22}$ ^{1}H homonuclear decoupling, $\tau = \tau' = 1.4$ ms) with GIPAW calculated chemical shifts overlaid as red crosses. Right panel: A schematic representation of the DFT geometry optimized structure of **G** illustrating the N−H···N and N−H···O intermolecular hydrogen bonding interactions and stating specific H−H proximities, (c) a ^{1}H (850 MHz, 75 kHz MAS) one-pulse spectrum, (d) a part of a ^{1}H DQ-SQ correlation spectrum (^{1}H 850 MHz, 75 kHz MAS using 1 τ_r of BABA recoupling), (e, f) ^{14}N−^{1}H HMQC spectra (^{1}H 850 MHz, 75 kHz MAS) for (e) a short (τ_{RCPL} = 106 μs) and (f) a longer (τ_{RCPL} = 533 μs) recoupling time. The base contour level is at (b) 1%, (d) 3%, (e) 12%, and (f) 12% of the maximum peak height.

guanosine derivatives; notably, ^{1}H and ^{15}N double-quantum (DQ) spectral patterns were used to assign quartet- and ribbon-like structures based on distinct intermolecular N−H···N and N−H···O hydrogen bonding interactions, including cases where it was not possible to obtain X-ray diffraction structures.[13,20,23] Figure 3 illustrates how a suite of one- and two-dimensional solid state MAS NMR spectra can be applied to characterize ribbon-like self-assembly in **G**. Similar NMR spectra have been presented for **dG(C3)$_2$** and **Gace** in previous studies.[20,23] The ^{1}H and ^{13}C cross-polarization (CP) MAS one-dimensional NMR spectra of **G** shown in Figure 3 directly indicate that there are two crystallographically independent molecules in the asymmetric unit cell ($Z' = 2$), via a clear observation of a pair of signals for the NH1 and C8 chemical sites. A two-dimensional heteronuclear ^{1}H−^{13}C correlation experiment (Figure 3b) was performed to assign the C−H pairs, i.e., protons directly bonded to carbons. In the ^{1}H−^{13}C refocused INEPT spectrum, 12 C−H correlations were clearly observed, further indicating that there are two crystallographically independent molecules.

Specific correlations observed in the region of the ^{1}H DQ-SQ (single-quantum) correlation spectrum corresponding to the N−H···N and N−H···O protons are evident in Figure 3d. The full ^{1}H DQ-SQ correlation spectrum is presented in Figure S2 in the Supporting Information. DQ peaks appear at the sum of the SQ peaks:[31,48,49] the δ_{DQ} peaks at 19.8 ppm (δ_{SQ}, 12.1 + δ_{SQ}, 7.7) and at 20.9 ppm (13.1 + 7.8) are assigned to NH1A−H8A and NH1B−H8B correlations, respectively; similarly, the δ_{DQ} peaks at 18.4 ppm (12.1 + 6.3) and at 19.9 ppm (13.1 + 6.8) are assigned to NH1A−NH$_{2b}$A and NH1B−NH$_{2b}$B correlations, respectively. In addition, N−H proximities are probed through ^{1}H−^{14}N HMQC spectra (^{14}N, I = 1, 99.6%) recorded using n = 2 rotary resonance recoupling[50] (R^3) of the heteronuclear dipolar couplings.[51−56] It is apparent from Figure 3e that one-bond N−H correlations are solely observed for the shorter recoupling time, 106 μs, while longer-range correlations appear for the longer recoupling time, 533 μs (Figure 3f), notably between H8 and N7 and N9.

A GIPAW DFT calculation of NMR chemical shieldings was performed for **G** (see Table S1 in the Supporting Information for a listing of the GIPAW DFT calculated and experimental ^{1}H and ^{13}C chemical shifts, as well as Figure S1, whereby the experimentally observed NMR chemical shifts are plotted against GIPAW calculated NMR chemical shieldings). A stick

DOI: 10.1021/acs.cgd.5b01440
Cryst. Growth Des. 2015, 15, 5945−5954

spectrum of GIPAW calculated ^{13}C chemical shifts is plotted on top of the experimental ^{13}C CP MAS spectrum (Figure 3a), and the GIPAW calculated chemical shifts for C−H pairs as overlaid using red crosses in the $^{13}C-^{1}H$ spectrum (Figure 3b) show a reasonably good agreement between experimental and DFT calculated chemical shifts. For the DFT geometry optimized structure of **G** shown in Figure 3, the H−H distances are indicated together with the intermolecular NH···N and NH···O hydrogen bonding distances. GIPAW calculated chemical shieldings have been reported for **dG(C3)$_2$** and **Gace** in previous studies.[20,23] For all molecules, the GIPAW calculated ^{14}N chemical shifts together with the quadrupolar NMR parameters are also listed in Table S2 of the Supporting Information.

Molecule to Full Crystal: GIPAW DFT Calculations Probe the Role of Noncovalent Interactions in Ribbon-like Guanosine Self-Assembly. The above section has shown that there is a good agreement between the GIPAW calculated and experimental NMR chemical shifts for **G**. This section shows how the effect of intermolecular interactions on NMR chemical shifts can be analyzed by comparing NMR chemical shieldings calculations performed for the full crystal (i.e., wherein all intermolecular interactions are present) versus those for extracted isolated molecules (i.e., in the absence of intermolecular interactions). Similar calculations have been performed on a wide range of organic molecules including compounds exhibiting weak CH···O and CH···N hydrogen bonding interactions,[24,26] amino acids,[25] a camphor derivative,[57] carbazole functionalized isocyanides,[28] and pharmaceuticals.[29,30,32,33] Relative changes in the GIPAW calculated NMR chemical shifts between the full crystal and extracted molecules $\Delta\delta_{iso}^{C-M}$ are investigated here. For ^{1}H nuclei in **G**, **dG(C3)$_2$**, and **Gace**, the cases where $\Delta\delta_{iso}^{C-M}$ values are ≥2 ppm are plotted in Figure 4 (see Table S3 in the Supporting Information for a full

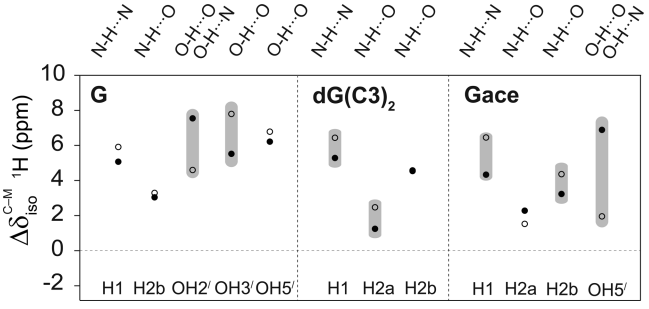

Figure 4. $\Delta\delta_{iso}^{C-M}$ (see eq 1) values are plotted for the two crystallographically independent molecules A (filled circles) and B (hollow circles) for the ^{1}H nuclei in **G**, **dG(C3)$_2$**, and **Gace**. Data are only presented for those chemical sites for which $\Delta\delta_{iso}^{C-M} \geq 2$ ppm for either or both molecules. Gray vertical shading highlights differences of more than 1 ppm.

listing of the calculated chemical shielding tensors for the full crystal and extracted molecules):

$$\Delta\delta_{iso}^{C-M} = \delta_{iso}^{\text{full crystal}} - \delta_{iso}^{\text{extracted molecule}} \quad (1)$$

Considering Figure 4, in all cases, the larger deviations in the $\Delta\delta_{iso}^{C-M}$ values for H1 and H2b are accounted by intermolecular N−H1···N7 and N−H2b···O6 hydrogen bonding interactions. This analysis reveals that the imino (H1) protons are involved in strong N−H···N hydrogen bonds for which the $\Delta\delta_{iso}^{C-M}$ values are typically larger, 4.3−6.5 ppm, followed by those for the amino (H2b) protons that form relatively weaker N−H···O hydrogen bonds resulting in changes in $\Delta\delta_{iso}^{C-M}$ values between 3 and 4.6 ppm. This is also mirrored in Table 1 wherein longer donor−acceptor distances and deviations up to 27° from linearity of hydrogen bonding angles are observed for the N−H···O interactions. Note that the $\Delta\delta_{iso}^{C-M}$ values of H2b protons are superimposed in **dG(C3)$_2$** due to the similar strengths of N−H2b···O6 interactions for both A and B molecules, which is consistent with their identical donor−acceptor distances, 2.86 Å, as presented in Table 1.

In **G**, changes observed in the $\Delta\delta_{iso}^{C-M}$ values for the OH2′, OH3′, and OH5′ protons (Figure 4) can be explained by means of intermolecular interactions between guanosine molecules and with water molecules. As illustrated in Figure 5, the OH2′(B)···N3(A), 2.95 Å hydrogen bonding interactions are connecting molecules A and B in neighboring ribbons along the crystallographic axis, *a* (top view, green color shading), while inter-ribbon OH2′(A)···O5′(A), 2.74 Å, hydrogen bonds are observed between two A molecules in neighboring ribbons along the crystallographic axis, *c* (side view, gray shading). In addition, inter- (W1 and W2) and intralayer (W3 and W4) water molecules are strongly interconnecting guanosine molecules in neighboring ribbons by means of an extended network of hydrogen bonding interactions. This extended network of hydrogen bonding interactions is visually represented in the expanded region of Figure 5 (top view, gray colored shading); OH3′(A), O3′(B), and O5′(B) groups are interconnected by an interlayer W2 water molecule (lower half of the gray shading), which is further connected to a nearby interlayer W1 water molecule bridged between OH3′(B) and O3′(A) groups (upper half of the gray shading). Note that the oxygen atom of W2 is shared between OH3′(B)···O(W2) and O(W2)···H_2O(W1) hydrogen bonds; i.e., O(W2) is involved in bifurcated hydrogen bonds, while the two hydrogen atoms of W2 participate in OH(W2)···O3′(B), 2.78 Å and OH(W2)···O5′(B), 2.74 Å hydrogen bonds. In the extended network of OH3′(B)···OH_2(W1)···OH_2(W2)···OH5′(B) hydrogen bonds, the donor−acceptor distances of OH3′(B)···O(W1) and OH(W2)···O5′(B) hydrogen bonds are 2.63 and 2.74 Å, respectively. By comparison in the OH3′(A)···OH_2(W2)···OH_2(W1)···OH3′(A) hydrogen bonding network, the donor−acceptor distances in OH3′(A)···O(W2) and OH(W1)···O3′(A) hydrogen bonds are 2.82 and 2.80 Å, respectively. Furthermore, the expanded region of Figure 5 (top view, magenta shading) represents the hydrogen bonds formed by intralayer W3 water molecules interconnecting two A molecules in the neighboring ribbons via OH2′(A)···OH_2(W3)···O6′(A) hydrogen bonds for which donor−acceptor distances are 2.68 and 2.89 Å, respectively. The intralayer W4 water is connecting two B type molecules in the neighboring ribbons via OH5′(B)···OH_2(W4)···O6′(B) interactions for which donor−acceptor distances are 2.74 and 2.98 Å (Figure 5, dashed square). Oxygen atoms of W3 and W4 water molecules are involved in bifurcated hydrogen bonds and they are interconnected by means of OH(W4)···O(W3), 2.80 Å hydrogen bonds. Figure 5 (broken square) also shows that the free amino protons H2a of both A and B type molecules are interacting with intralayer water molecules by means of NH2a(B)···O, 3.07 Å and NH2a(A)···O, 2.90 Å hydrogen bonds.

The $\Delta\delta_{iso}^{C-M}$ values of OH2′ protons differ by almost 4 ppm because of the different nature of hydrogen bonding interactions for the A and B molecules, i.e., OH2′(B)···

DOI: 10.1021/acs.cgd.5b01440
Cryst. Growth Des. 2015, 15, 5945−5954

Table 1. Hydrogen Bonding Donor−Acceptor[a] Distances and Angles As Obtained from the DFT Geometry Optimized Structures

donor and acceptor (X and Y)	hydrogen bonding distance (X···Y), in Å			hydrogen bonding angle (XHY), in deg		
	G	**dG(C3)$_2$**	**Gace**	**G**	**dG(C3)$_2$**	**Gace**
N−H1···N7	2.85 (A→A)	2.93 (A→B)	2.84 (A→B)	178.6 (A→A)	177.7 (A→B)	174.1 (A→B)
N−H1···N7	2.79 (B→B)	2.87 (B→A)	2.80 (B→A)	179.6 (B→B)	178.7 (B→A)	170.4 (B→A)
N−H2b···O6	2.92 (A→A)	2.86 (A→B)	2.92 (A→B)	156.9 (A→A)	158.2 (A→B)	153.3 (A→B)
N−H2b···O6	2.87 (B→B)	2.86 (B→A)	2.87 (B→A)	153.3 (B→B)	159.5 (B→A)	159.9 (B→A)
N−H2a···O8′		3.13 (A→B)[b]			128.3 (A→B)[b]	
N−H2a···O8′		2.99 (B→B)			155.7 (B→B)	
N−H2a···O	2.90 (A→W3)			115.7 (A→W3)		
N−H2a···O	3.07 (B→W4)		3.22 (B→W1)	122.5 (B→W4)		163.9 (B→W1)
O−H2′···O5′	2.74 (A→A)[b]			173.5 (A→A)[b]		
O−H3′···O	2.63 (B→W1)			164.3 (B→W1)		
O−H3′···O	2.82 (A→W2)			173.6 (A→W2)		
O−H5′···O5′			2.67 (A→B)[b]			161.9 (A→B)[b]
O−H5′···O	2.70 (B→W4)			168.0 (B→W4)		
O−H···O2′	2.68 (W3→A)			163.6 (W3→A)		
O−H···O3′	2.80 (W1→A)			174.0 (W1→A)		
O−H···O3′	2.78 (W2→B)			179.9 (W2→B)		
O−H···O5′	2.74 (W2→B)		2.72 (W1→A)	170.2 (W2→B)		166.0 (W1→A)
O−H···O6	2.89 (W3→A)			121.0 (W3→A)		
O−H···O6	2.98 (W4→B)			155.0 (W4→B)		
O−H···O	2.78 (W1→W2)			172.3 (W1→W2)		
O−H···O	2.80 (W4→W3)			173.8 (W4→W3)		
O−H2′···N3	2.95 (B→A)[b]			166.7 (B→A)[b]		
O−H5′···N3	2.80 (A→B)[b]		2.68 (B→B)[c]	161.9 (A→B)[b]		170.2 (B→B)[c]

[a]The symbol → represents the directionality of the hydrogen bonding interaction, with the arrow pointing toward an acceptor site. An overview of molecular packing in **G**, **dG(C3)$_2$** and **Gace** is shown in Figure 1. Hydrogen bonding donor and acceptor moieties in A and B ribbons and water (W) molecules are identified. [b]Inter-ribbon hydrogen bonding interactions between guanosine molecules. [c]Intramolecular hydrogen bonds within the same ribbon.

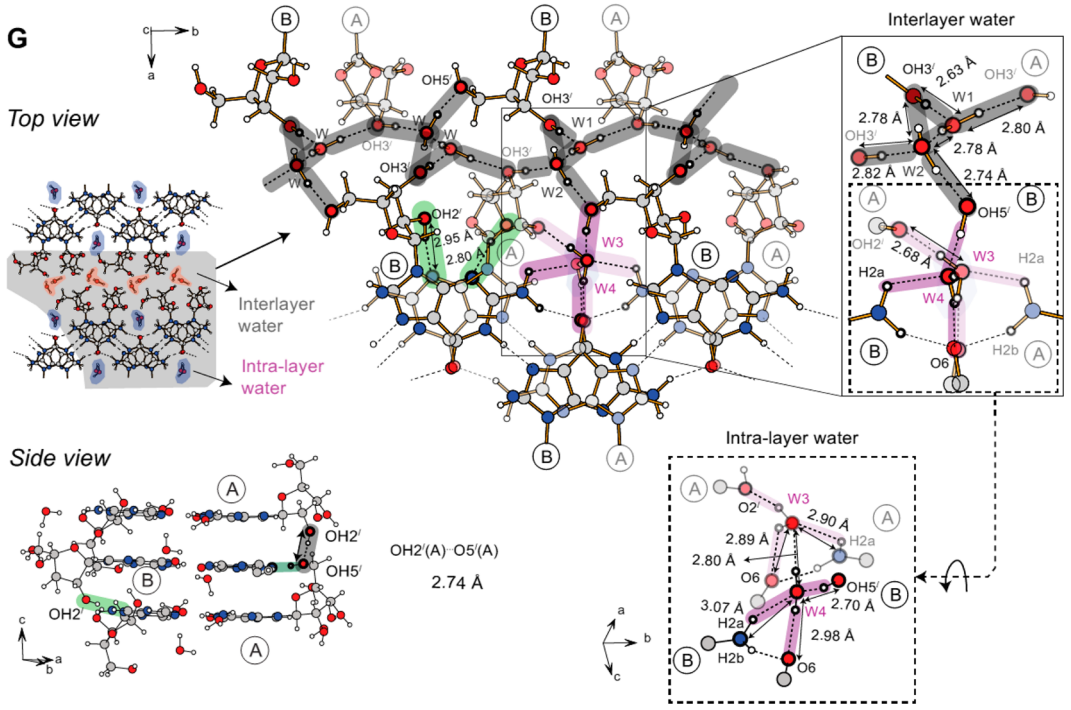

Figure 5. Overview of intermolecular interactions **G** that lead to the differences in the $\Delta\delta_{iso}^{C-M}$ ^{1}H (ppm) values presented in Figure 4. Insets in the top panels highlight the hydrogen bonding interactions between **G** and interlayer water molecules, and between **G** and intralayer water molecules. The side view (bottom left) depicts interlayer O−H···O interactions between A-type molecules.

DOI: 10.1021/acs.cgd.5b01440
Cryst. Growth Des. 2015, 15, 5945−5954

Table 2. GIPAW DFT Calculated NMR ^{1}H Chemical Shifts for Water Protons in G, Together with Their Hydrogen Bonding Interactions

donor and acceptor (X and Y)	δ_{calc} ^{1}H (ppm)	hydrogen bonding distance (X···Y), in Å	hydrogen bonding angle (XHY), in deg
W1			
O−H(W1)···O3′(A)	5.3	2.80 (W1→A)	174.0 (W1→A)
O−H(W1)···O(W2)	6.2	2.78 (W1→W2)	172.3 (W1→W2)
W2			
O−H(W2)···O5′(B)	7.3	2.74 (W2→B)	170.2 (W2→B)
O−H(W2)···O3′(B)	6.6	2.78 (W2→B)	179.9 (W2→B)
W3			
O−H(W3)···O2′(A)	6.4	2.68 (W3→A)	163.6 (W3→A)
O−H(W3)···O6(A)	0.9	2.89 (W3→A)	121.0 (W3→A)
W4			
O−H(W4)···O6(B)	2.1	2.98 (W4→B)	155.0 (W4→B)
O−H(W4)···O(W3)	6.2	2.80 (W4→W3)	173.8 (W4→W3)

N3(A), 2.95 Å and OH2′(A)···O5′(A), 2.74 Å intermolecular interaction. Furthermore, only hydrogens of hydroxyl groups at the 3′ position of B molecules are involved in an extended hydrogen bonding network with water molecules OH3′(B)···OH_2(W1)···OH_2(W2)···OH5′(B), while both hydrogens and oxygen atoms of hydroxyl groups at the 3′ position of A molecules are interacting with the water molecules OH3′(A)···O(W2) and OH(W1)···O3′(A). The OH3′(A)···O(W2) and OH3′(B)··· O(W1) distances are 2.82 and 2.63 Å respectively, hence explaining a nearly 2.5 ppm difference in the $\Delta\delta_{iso}^{C-M}$ values for OH3′ protons of the A and B molecules. The $\Delta\delta_{iso}^{C-M}$ values of OH5′ protons are different due to inter-ribbon OH5′(A)···N3(B), 2.80 Å hydrogen bonds (Figure 5, green shading) and OH5′(B)···O(W4), 2.70 Å hydrogen bonds with an interlayer water (W4) molecule (Figure 5, magenta shading). The $\Delta\delta_{iso}^{C-M}$ values of OH2′, OH3′, and OH5′ also show that the O−H···O interactions are as strong as, and even stronger than N−H···N, N−H···O, and O−H···N interactions, with this being mirrored in the shorter donor−acceptor distances and the linearity of hydrogen bonding angles listed in Table 1. Table 2 presents an analysis of the hydrogen-bonding interactions adopted by the four water molecules. Table 2 also lists the GIPAW calculated ^{1}H chemical shifts; it is clear that the anomalous low values for one of the OH groups in both a W3 and a W4 water molecule are a consequence of weaker OH···O hydrogen bonding (distances greater than 2.8 Å and bond angles less than 160°). Note that there is insufficient resolution in this region of the ^{1}H DQ-SQ MAS spectrum (see Figure S2) to identify these chemical shifts experimentally. In conclusion, it is evident that the hydrogen bonding networks formed by the inter- and intralayer water molecules shown in Figure 5 are crucial for holding together the three-dimensional ribbons in **G**.

In **dG(C3)$_2$**, the substitution with short alkyl chains causes a steric hindrance between successive ribbons with each ribbon being surrounded by alkyl chains as shown in Figure 6 (side view). The amino protons are involved in intermolecular N−H2a(B)···O8′(B) hydrogen bonds that link together adjacent B molecules within the same ribbon (top view of Figure 6, gray shading). The amino protons in the type A molecule form similar hydrogen bonds with O8′(B) in the neighboring ribbon, N−H2a(A)···O8′(B) (Figure 6, side view−gray shading), though the hydrogen-bonding distance is longer (3.13 Å as compared to 2.99 Å), resulting in a difference in the $\Delta\delta_{iso}^{C-M}$ values for H2a of nearly 2 ppm.

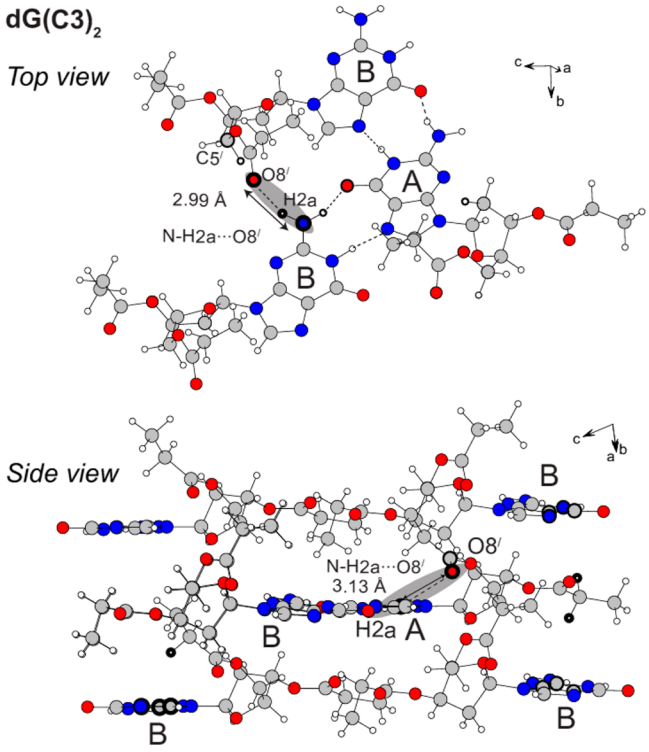

Figure 6. Overview of intermolecular NH···O hydrogen bonding interactions in **dG(C3)$_2$**.

Figure 7 illustrates intermolecular hydrogen bonding interactions observed for **Gace.** The amino proton H2a (B) forms N−H2a(B)···O(W1) hydrogen bonds with an interlayer water molecule, and this interlayer water forms O−H(W1)···O5′(A) hydrogen bonds with the neighboring ribbons (Figure 7, magenta shading). The donor−acceptor distances for the N−H2a(B)···O(W1) and O−H(W1)···O5′(A) interactions are 3.22 and 2.72 Å, respectively. Therefore, the interlayer water in **Gace** is interconnecting neighboring ribbons by means of N−H···O and O−H···O hydrogen bonds. In addition, inter-ribbon hydrogen bonding interactions are observed between OH5′(A)···O5′(B) groups for which the donor−acceptor distance is 2.67 Å. The OH5′(B) hydrogen exhibits intramolecular O−H5′(B)···N3(B), 2.68 Å, hydrogen bonding (Figure 7, gray shading). Changes observed in the $\Delta\delta_{iso}^{C-M}$ values for OH5′ protons in **Gace** are accounted by the difference in the nature of molecular interactions, herein,

DOI: 10.1021/acs.cgd.5b01440
Cryst. Growth Des. 2015, 15, 5945−5954

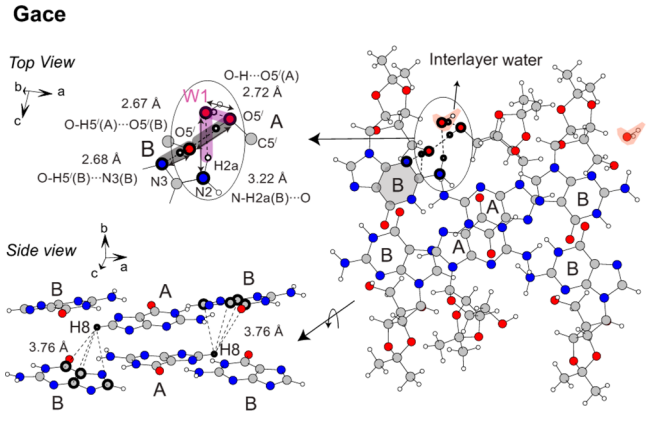

Figure 7. Overview of inter and intramolecular hydrogen bonding interactions (top) and CH−π interactions (bottom) in **Gace**.

intermolecular OH5′(A)···O5′(B) hydrogen bonds and intramolecular OH5′(B)···N3 and OH5′(B)-π interactions with the guanine skeleton. As described in a previous study,[23] the difference in the ^{1}H chemical shifts for the H8 protons in the A and B molecules can be explained by means of CH−π interactions between H8(A) and the purine base of B type molecules in the neighboring ribbons (Figure 7, side view).

On the basis of the interpretation of the stem plots presented in Figure 4 and the observation of inter- and intramolecular interactions shown in Figures 5, 6, and 7, it can be inferred that the N−H···N, N−H···O, O−H···O, O−H···N hydrogen bonding interactions, and CH−π interactions significantly stabilize the ribbon-like structures in a cooperative manner.

Sugar Conformations. For the two crystallographically independent molecules in each guanosine derivative studied here, the sugar conformations are respectively *syn* and *anti* in **G**, both are *anti* in **dG(C3)$_2$** and both are *syn* in **Gace**, as characterized by the C4−N9−C1′−O6′ dihedral angles in the DFT optimized structures (Figure 8). The C4−N9−C1′−O6′

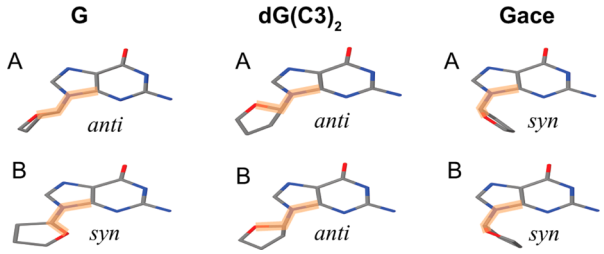

Figure 8. Sugar conformations in **G**, **dG(C3)$_2$**, and **Gace** obtained from GIPAW DFT geometry structures. Color legend of atoms: C (gray), N (blue), and O (red). The dihedral angle connecting C4−N9−C1′−O6′ is highlighted. Functional groups at 2′, 3′, and 5′ are omitted to facilitate a clearer visual representation. For all molecules, the torsion angles measured across the N-glycosidic bonds and for the furanose ring carbons are listed in Table S4 in the Supporting Information, and the experimental C8 NMR chemical shifts are listed in Table 3.

dihedral angle for A and B molecules are respectively −138.5° and −58.3° in **G**, −157.1° and −133.8° in **dG(C3)$_2$**, and 81.3° and 72.1° in **Gace**. Previous work has shown that the ^{13}C C8 chemical shift values are known to be measurably different for syn- and anti-conformers in **dG(C3)$_2$** and in **Gace** (see Table 5 of ref 20). For **G**, **dG(C3)$_2$**, and **Gace**, the ^{13}C chemical shift values for the two crystallographically independent molecules are presented in Table 3. It is thus evident that a ^{13}C C8 chemical shift above or below 135 ppm is characteristic of a

Table 3. Experimental ^{13}C NMR Chemical Shifts for C8

		experimental chemical shift in ppm		
chemical site	type	**G**	**dG(C3)$_2$**	**Gace**
C8	A	131.7 "*anti*"	132.9 "*anti*"	136.0 "*syn*"
	B	138.1 "*syn*"	134.2 "*anti*"	137.4 "*syn*"

syn- or an anti-conformation, respectively. In addition, torsion within the furanose ring is characterized by means of torsional angles measured across specific dihedrals for the DFT optimized structures and for X-ray diffraction structures. These torsional angles are reported in Table S4 in the Supporting Information.

CONCLUSIONS

This study has probed similarities and differences in the ribbon-like supramolecular structures for three guanosine derivatives in the solid state. A NMR crystallography approach has been employed to quantitatively unravel the role of specific intermolecular interaction by means of GIPAW DFT calculated NMR chemical shifts on full crystal vs isolated molecules for the two crystallographically independent molecules in each guanosine derivative. The NMR crystallography analysis reveals that intermolecular interactions are differently experienced for the two crystallographically independent molecules. In particular, GIPAW calculations performed on full crystal versus extracted isolated molecules show that intermolecular N−H···N hydrogen bonds are stronger than the N−H···O hydrogen bonds, corresponding also to shorter donor−acceptor distances and an increased linearity of the hydrogen bonding angles. In addition to the N−H···N and N−H···O hydrogen bonds which are interconnecting guanosine units, several other noncovalent interactions such as O−H···N, O−H···O, and CH−π interactions contribute to stabilizing the overall three-dimensional structures in a cooperative manner. For the ribbon-like structures studied here, a diversity in hydrogen bonding interactions can be seen.

For **G** and **Gace**, NMR crystallography is complemented by thermal analysis that shows that **G** is a dihydrate and **Gace** is a hemihydrate. The presence of lattice water reinforces stacking of two-dimensional molecular sheets in **G** and **Gace**. In **G**, two interlayer water molecules are interconnecting sugar rings and two intralayer water molecules are connecting guanine frames in the neighboring ribbons by means of an extended hydrogen bonding network. For the three guanosine derivatives studied here, the base-sugar conformations are both *syn* and *anti* in **G**, all *anti* in **dG(C3)$_2$** and all syn in **Gace**. It is shown that the ^{13}C C8 chemical shift (above or below 135 ppm) is diagnostic of a syn or an anti-conformation.

To conclude, this study has demonstrated the power of a NMR crystallography approach for a detailed study of the interplay of noncovalent interactions governing supramolecular self-assembly; further applications within materials chemistry are to be envisaged.[58]

EXPERIMENTAL AND COMPUTATIONAL DETAILS

G was purchased from Sigma-Aldrich (Gillingham, UK), recrystallized from water, and vacuum-dried prior to thermal analysis. Recrystallized **G** was subjected to solid-state NMR characterization.

DOI: 10.1021/acs.cgd.5b01440
Cryst. Growth Des. 2015, 15, 5945−5954

Thermal Analysis. Thermogravimetric analysis (TGA) was performed using a TA Q5000 instrument. Approximately 6 mg of sample was placed in an aluminum sample holder and heated over the temperature range 25−200 °C at a constant heating rate of 10 °C per minute. Helium gas was employed as a purge gas at a flow rate of 50 mL per minute.

Solid-State NMR. 56.2 mg and 0.6 mg of **G** were packed into a Bruker 4 mm and a JEOL 1.0 mm (outer diameter) rotor, respectively. Solid-state NMR experiments were performed at room temperature using either a 11.7 T (^{1}H Larmor frequency, 500 MHz) Bruker Avance III, 14.1 T (^{1}H Larmor frequency, 600 MHz) Bruker Avance II+, or a 20 T (^{1}H Larmor frequency, 850 MHz) Bruker Avance III spectrometer equipped with a Bruker 4 mm HXY (tuned into double resonance mode) or a JEOL 1 mm HX probe.

^{13}C CPMAS. A ^{13}C CPMAS spectrum of **G** was acquired using the 500 MHz spectrometer with a 4 mm rotor spinning at 10 kHz. The ^{13}C 90° pulse duration was 4.0 μs and the ^{1}H nutation frequency was 100 kHz. Cross-polarization was achieved using an r.f. pulse ramped from 70 to 100% on the ^{1}H channel with a contact time of 1 ms. ^{1}H heteronuclear decoupling was applied during acquisition using SPINAL64 heteronuclear decoupling[59] with a pulse duration of 5 μs. 2048 transients were coadded with a 3 s recycle delay, corresponding to a total experimental time of nearly 2 h.

^{1}H−^{13}C Refocused INEPT. A ^{1}H−^{13}C heteronuclear correlation spectrum of **G** was recorded using the 600 MHz spectrometer with a 4 mm triple resonance probe HXY tuned into double resonance mode. The refocused-INEPT[60] (insensitive nuclei enhancement using polarization transfer) pulse sequence with eDUMBO-1$_{22}$ homonuclear decoupling[61] was applied to achieve high resolution in the indirect ^{1}H dimension. A short spin−echo duration time (1.2 ms) was used for the refocused INEPT transfer, so that correlation peaks are observed only for directly bonded ^{13}C−^{1}H pairs. For windowless eDUMBO-1$_{22}$, the homonuclear decoupling cycles were applied with a duration of 32 μs (320 steps of 100 ns each). Prepulses of duration 0.8 μs were used before and after the eDUMBO-1$_{22}$ pulses. The SPINAL64 ^{1}H heteronuclear decoupling scheme was used during acquisition with a pulse duration, 5 μs. The indirect dimension was acquired using 48 t_1 FIDs, each with 512 coadded transients, by using the States-TPPI method to achieve sign discrimination with an increment of 80 μs. The total experimental time was 17 h, with a recycle delay of 3 s. The ^{1}H chemical shifts are scaled in the F_1 dimension by a factor of 0.63.

^{1}H Double-Quantum (DQ) Spectroscopy. A DQ-SQ correlation spectrum of **G** was acquired using the 850 MHz spectrometer with a JEOL 1 mm HX probe. The MAS frequency was 75 kHz. One rotor period of the BABA[62,63] (back to back) recoupling sequence was used for the excitation and reconversion of DQ coherences. A 16-step phase cycle was used in order to select $\Delta p = \pm 2$ on the DQ excitation pulses (4 steps) and $\Delta p = -1$ (4 steps) on the z-filter 90° pulse, where p is the coherence order. 256 t_1 FIDs, each with 32 coadded transients, were acquired using the States method to achieve sign discrimination in the F_1 dimension with a rotor-synchronized t_1 increment of 13.3 μs, corresponding to an overall experimental time of 5 h using a 2 s recycle delay.

^{14}N−^{1}H HMQC. Experiments were performed on a Bruker Avance III spectrometer (^{1}H 850.2 MHz, ^{14}N 61.4 MHz) using a JEOL 1.0 mm HX probe at a MAS frequency of 75.0 kHz. A modified version of the pulse sequence due to Gan et al.[53] was employed to record ^{14}N−^{1}H HMQC spectra by applying a second ^{1}H 90° pulse (90° out of phase with respect to the first 90° pulse) immediately after the first ^{1}H 90° pulse and using phase inversion (every rotor period) of the $n = 2$ ($\nu_1 = 2\ \nu_R$) rotary-resonance recoupling pulses.[55] A four-step nested phase cycle was used to select changes in coherence order $\Delta p = \pm 1$ (on the first ^{1}H pulse, 2 steps) and $\Delta p = -1$ (on the last ^{14}N pulse, 2 steps). The ^{1}H and ^{14}N 90° pulse durations were 2 and 5 μs, respectively. For each of 48 t_1 FIDs (using the States method to achieve sign discrimination in F_1 with a rotor synchronized increment of 13.3 μs), 128 transients were coadded with a recycle delay of 2 s corresponding to a total experimental time of 4 h.

All ^{1}H and ^{13}C experimental shifts are calibrated with respect to neat TMS using adamantane as an external reference (higher ppm ^{13}C resonance, 35.8 ppm[64] and the ^{1}H resonance, 1.85 ppm[65]). ^{14}N chemical shifts were referenced to a saturated NH_4Cl aqueous solution at −352.9 ppm, corresponding to the primary reference, liquid CH_3NO_2 (0 ppm). To compare to the alternative reference of liquid NH_3 at −50 °C as used in protein NMR, it is necessary to add 379.5 ppm.[66]

GIPAW DFT Calculations. Calculations were performed at the Warwick Centre for Scientific Computing using plane-wave based DFT approaches[67,68] implemented in the CASTEP code, UK academic release version 6.1.[69] Initial atomic coordinates were taken from published crystal structures: **G,** Guanosine dihydrate,[5] CSD code GUANSH10, $Z = 4$, $Z' = 2$, space group $P2_1$, 156 atoms/cell (including 8 H_2O); **dG(C3)$_2$**, 3′,5′-*O*-dipropanolyl deoxyguanosine,[9] CSD code MOFBUE, $Z = 2$, $Z' = 2$, space group $P1$, 96 atoms/cell; **Gace,** 2′,3′-*O*-isopropylidineguanosine,[6] CSD code VUYMIL, $Z = 4$, $Z' = 2$, space group $P2_1$, 166 atoms/cell (including two H_2O). In all cases, the unit cell parameters were fixed, the space group symmetry was imposed, and periodic boundary conditions were applied during the geometry optimization. NMR shielding calculations of **G**, **dG(C3)$_2$**, and **Gace** were performed using the gauge-including projector-augmented wave (GIPAW) approach.[67,68] Both geometry optimizations and NMR chemical shift calculations used a plane-wave basis set and the PBE exchange correlation functional[70] at a basis cutoff energy of 600 eV with integrals taken over the Brillouin zone by using a Monkhorst−Pack grid of minimum sample spacing 0.08 × 2π Å^{-1}. A semi empirical dispersion correction was applied using the TS scheme[71] in both geometry optimization and NMR shielding calculations with on-the-fly (OTF) ultrasoft pseudopotentials.[72] In all cases, forces, stresses on the unit cells, energies, and displacements were converged to better than 0.01 eV Å^{-1}, 0.1 G Pa, 0.0000004 eV, and 0.001 Å, respectively. From the DFT geometry optimized crystal structures, single molecules (in each case A and B individually) are extracted and placed in a periodically repeating unit cell with dimensions: **G**, 17.52 × 23.00 × 13.32 Å^3; **dG(C3)$_2$**, 23.19 × 13.51 × 19.59 Å^3 and **Gace**, 17.81 × 20.65 × 21.95 Å^3, in order to separate the molecules in such a way that no two molecules are within a 8 Å distance. GIPAW calculations were performed on extracted single molecules using the above stated parameters. GIPAW calculated NMR shieldings of full cell and extracted molecules are viewed, processed, and tabulated through the CCP-NC output files visualization tool, MagresView.[73]

■ ASSOCIATED CONTENT

Ⓢ Supporting Information

The Supporting Information is available free of charge on the ACS Publications website at DOI: 10.1021/acs.cgd.5b01440.

Table and graphical plots of experimental vs GIPAW DFT calculated chemical shifts for **G**. For all molecules, tables of the NMR shielding parameters for the full crystal vs isolated molecules and the ^{14}N electric field gradient tensors and quadrupolar parameters. Full ^{1}H DQ-SQ MAS NMR spectrum. Table of torsional angles (PDF)

For all molecules, the .cif files and.magres files for the full crystal and isolated molecules (ZIP)

■ AUTHOR INFORMATION

Corresponding Author

*E-mail: S.P.Brown@warwick.ac.uk.

Notes

The authors declare no competing financial interest.

■ ACKNOWLEDGMENTS

We acknowledge funding from EPSRC (EP/K003674/1). The UK 850 MHz solid-state NMR Facility used in this research was funded by EPSRC and BBSRC, as well as the University of

DOI: 10.1021/acs.cgd.5b01440
Cryst. Growth Des. 2015, 15, 5945−5954

Warwick including via part funding through Birmingham Science City Advanced Materials Projects 1 and 2 supported by Advantage West Midlands (AWM) and the European Regional Development Fund (ERDF). We thank the 850 MHz Facility Manager, Dinu Iuga, for experimental assistance. Calculations were performed on the University of Warwick Centre for Scientific Computing (CSC) cluster. This work was performed within the framework of the EPSRC funded Collaborative Computational Project for NMR Crystallography (CCP-NC, EP/J010510/1). Helpful discussions with Jonathan Yates, University of Oxford, are gratefully acknowledged. The experimental thermal analysis and NMR data for this study are provided as a supporting dataset from WRAP, the Warwick Research Archive Portal at http://wrap.warwick.ac.uk/73969.

REFERENCES

(1) Aida, T.; Meijer, E. W.; Stupp, S. I. Functional Supramolecular Polymers. *Science* **2012**, *335*, 813−817.
(2) Chakrabarty, R.; Mukherjee, P. S.; Stang, P. J. Supramolecular Coordination: Self-Assembly of Finite Two- and Three-Dimensional Ensembles. *Chem. Rev.* **2011**, *111*, 6810−6918.
(3) Busseron, E.; Ruff, Y.; Moulin, E.; Giuseppone, N. Supramolecular self-assemblies as functional nanomaterials. *Nanoscale* **2013**, *5*, 7098−7140.
(4) González-Rodríguez, D.; Schenning, A. P. H. J. Hydrogen-bonded Supramolecular π-Functional Materials. *Chem. Mater.* **2011**, *23*, 310−325.
(5) Thewalt, U.; Bugg, C. E.; Marsh, R. E. The crystal structure of guanosine dihydrate and inosine dihydrate. *Acta Crystallogr., Sect. B: Struct. Crystallogr. Cryst. Chem.* **1970**, *26*, 1089−1101.
(6) Mande, S. S.; Seshadri, T. P.; Viswamitra, M. A. Structure of 2′,3′-O-isopropylideneguanosine hemihydrate. *Acta Crystallogr., Sect. C: Cryst. Struct. Commun.* **1989**, *45*, 92−94.
(7) Gottarelli, G.; Masiero, S.; Mezzina, E.; Pieraccini, S.; Rabe, J. P.; Samori, P.; Spada, G. P. The Self-Assembly of Lipophilic Guanosine Derivatives in Solution and on Solid Surfaces. *Chem. - Eur. J.* **2000**, *6*, 3242−3248.
(8) Forman, S. L.; Fettinger, J. C.; Pieraccini, S.; Gottarelli, G.; Davis, J. T. Toward Artificial Ion Channels: A Lipophilic G-Quadruplex. *J. Am. Chem. Soc.* **2000**, *122*, 4060−4067.
(9) Giorgi, T.; Grepioni, F.; Manet, I.; Mariani, P.; Masiero, S.; Mezzina, E.; Pieraccini, S.; Saturni, L.; Spada, G. P.; Gottarelli, G. Gel-Like Lyomesophases Formed in Organic Solvents by Self-Assembled Guanine Ribbons. *Chem. - Eur. J.* **2002**, *8*, 2143−2152.
(10) Sessler, J. L.; Sathiosatham, M.; Doerr, K.; Lynch, V.; Abboud, K. A. A G-Quartet Formed in the Absence of a Templating Metal Cation: A New 8-(*N*,*N*-dimethylaniline)guanosine Derivative. *Angew. Chem., Int. Ed.* **2000**, *39*, 1300−1303.
(11) Davis, J. T. G-Quartets 40 Years Later: From 5′-GMP to Molecular Biology and Supramolecular Chemistry. *Angew. Chem., Int. Ed.* **2004**, *43*, 668−698.
(12) Sreenivasachary, N.; Lehn, J. M. Gelation-driven component selection in the generation of constitutional dynamic hydrogels based on guanine-quartet formation. *Proc. Natl. Acad. Sci. U. S. A.* **2005**, *102*, 5938−5943.
(13) Pham, T. N.; Masiero, S.; Gottarelli, G.; Brown, S. P. Identification by ^{15}N Refocused INADEQUATE MAS NMR of Intermolecular Hydrogen Bonding that Directs the Self-Assembly of Modified DNA Bases. *J. Am. Chem. Soc.* **2005**, *127*, 16018.
(14) Davis, J. T.; Spada, G. P. Supramolecular architectures generated by self-assembly of guanosine derivatives. *Chem. Soc. Rev.* **2007**, *36*, 296−313.
(15) Martić, S.; Liu, X. Y.; Wang, S. N.; Wu, G. Self-Assembly of N2-Modified Guanosine Derivatives: Formation of Discrete G-Octamers. *Chem. - Eur. J.* **2008**, *14*, 1196−1204.
(16) Gonzalez-Rodriguez, D.; van Dongen, J. L. J.; Lutz, M.; Spek, A. L.; Schenning, A.; Meijer, E. W. G-quadruplex self-assembly regulated by Coulombic interactions. *Nat. Chem.* **2009**, *1*, 151−155.
(17) Li, M.; Oakley, R. J.; Bevan, H.; Smarsly, B. M.; Mann, S.; Faul, C. F. J. Nucleotide-based Templates for Nanoparticle Production: Exploiting Multiple Noncovalent Interactions. *Chem. Mater.* **2009**, *21*, 3270−3274.
(18) Ciesielski, A.; Lena, S.; Masiero, S.; Spada, G. P.; Samorì, P. Dynamers at the Solid−Liquid Interface: Controlling the Reversible Assembly/Reassembly Process between Two Highly Ordered Supramolecular Guanine Motifs. *Angew. Chem., Int. Ed.* **2010**, *49*, 1963−1966.
(19) Simeone, L.; Milano, D.; De Napoli, L.; Irace, C.; Di Pascale, A.; Boccalon, M.; Tecilla, P.; Montesarchio, D. Design, Synthesis and Characterisation of Guanosine-Based Amphiphiles. *Chem. - Eur. J.* **2011**, *17*, 13854−13865.
(20) Webber, A. L.; Masiero, S.; Pieraccini, S.; Burley, J. C.; Tatton, A. S.; Iuga, D.; Pham, T. N.; Spada, G. P.; Brown, S. P. Identifying Guanosine Self Assembly at Natural Isotopic Abundance by High-Resolution ^{1}H and ^{13}C Solid-State NMR Spectroscopy. *J. Am. Chem. Soc.* **2011**, *133*, 19777−19795.
(21) Peters, G. M.; Skala, L. P.; Plank, T. N.; Hyman, B. J.; Reddy, G. N. M.; Marsh, A.; Brown, S. P.; Davis, J. T. A G_4·K+ Hydrogel Stabilized by an Anion. *J. Am. Chem. Soc.* **2014**, *136*, 12596−12599.
(22) Peters, G. M.; Skala, L. P.; Plank, T. N.; Oh, H.; Manjunatha Reddy, G. N.; Marsh, A.; Brown, S. P.; Raghavan, S. R.; Davis, J. T. G_4-Quartet·M+ Borate Hydrogels. *J. Am. Chem. Soc.* **2015**, *137*, 5819−5827.
(23) Reddy, G. N. M.; Cook, D. S.; Iuga, D.; Walton, R. I.; Marsh, A.; Brown, S. P. A NMR Crystallography Study of the Hemihydrate of 2′, 3′-O-Isopropylidineguanosine. *Solid State Nucl. Magn. Reson.* **2015**, *65*, 41−48.
(24) Yates, J. R.; Pham, T. N.; Pickard, C. J.; Mauri, F.; Amado, A. M.; Gil, A. M.; Brown, S. P. An Investigation of Weak CH···O Hydrogen Bonds in Maltose Anomers by a Combination of Calculation and Experimental Solid-State NMR Spectroscopy. *J. Am. Chem. Soc.* **2005**, *127*, 10216−10220.
(25) Schmidt, J.; Hoffmann, A.; Spiess, H. W.; Sebastiani, D. Bulk Chemical Shifts in Hydrogen-Bonded Systems from First-Principles Calculations and Solid-State-NMR. *J. Phys. Chem. B* **2006**, *110*, 23204−23210.
(26) Uldry, A. C.; Griffin, J. M.; Yates, J. R.; Perez-Torralba, M.; Santa Maria, M. D.; Webber, A. L.; Beaumont, M. L. L.; Samoson, A.; Claramunt, R. M.; Pickard, C. J.; Brown, S. P. Quantifying Weak Hydrogen Bonding in Uracil and 4-Cyano-4′-ethynylbiphenyl: A Combined Computational and Experimental Investigation of NMR Chemical Shifts in the Solid State. *J. Am. Chem. Soc.* **2008**, *130*, 945−954.
(27) Brouwer, D. H.; Alavi, S.; Ripmeester, J. A. NMR crystallography of p-tert-butylcalix[4]arene host−guest complexes using ^{1}H complexation-induced chemical shifts. *Phys. Chem. Chem. Phys.* **2008**, *10*, 3857−3860.
(28) Gowda, C. M.; Vasconcelos, F.; Schwartz, E.; van Eck, E. R. H.; Marsman, M.; Cornelissen, J.; Rowan, A. E.; de Wijs, G. A.; Kentgens, A. P. M. Hydrogen bonding and chemical shift assignments in carbazole functionalized isocyanides from solid-state NMR and first-principles calculations. *Phys. Chem. Chem. Phys.* **2011**, *13*, 13082−13095.
(29) Bradley, J. P.; Velaga, S. P.; Antzutkin, O. N.; Brown, S. P. Probing Intermolecular Crystal Packing in γ-Indomethacin by High-Resolution ^{1}H Solid-State NMR Spectroscopy. *Cryst. Growth Des.* **2011**, *11*, 3463−3471.
(30) Mafra, L.; Santos, S. M.; Siegel, R.; Alves, I.; Almeida Paz, F. A.; Dudenko, D.; Spiess, H. W. Packing interactions in hydrated and anhydrous forms of the antibiotic Ciprofloxacin: a solid-state NMR, X-ray diffraction, and computer simulation study. *J. Am. Chem. Soc.* **2012**, *134*, 71−74.
(31) Brown, S. P. Applications of high-resolution ^{1}H solid-state NMR. *Solid State Nucl. Magn. Reson.* **2012**, *41*, 1−27.

DOI: 10.1021/acs.cgd.5b01440
Cryst. Growth Des. 2015, 15, 5945−5954

(32) Dudenko, D. V.; Williams, P. A.; Hughes, C. E.; Antzutkin, O. N.; Velaga, S. P.; Brown, S. P.; Harris, K. D. M. Exploiting the Synergy of Powder X-ray Diffraction and Solid-State NMR Spectroscopy in Structure Determination of Organic Molecular Solids. *J. Phys. Chem. C* **2013**, *117*, 12258−12265.
(33) Dudenko, D. V.; Yates, J. R.; Harris, K. D. M.; Brown, S. P. An NMR crystallography DFT-D approach to analyse the role of intermolecular hydrogen bonding and $\pi-\pi$ interactions in driving cocrystallisation of indomethacin and nicotinamide. *CrystEngComm* **2013**, *15*, 8797−8807.
(34) Harris, R. K. NMR studies of organic polymorphs & solvates. *Analyst* **2006**, *131*, 351−373.
(35) Elena, B.; Pintacuda, G.; Mifsud, N.; Emsley, L. Molecular Structure Determination in Powders by NMR Crystallography from Proton Spin Diffusion. *J. Am. Chem. Soc.* **2006**, *128*, 9555−9560.
(36) Harris, R. K.; Wasylishen, R. E.; Duer, M. J. *NMR Crystallography*; Wiley: Chichester, 2009.
(37) Gottarelli, G.; Masiero, S.; Mezzina, E.; Pieraccini, S.; Spada, G. P.; Mariani, P. A new lyotropic liquid crystalline phase formed in hydrocarbon solvents bya deoxyguanosine derivative through extensive hydrogen bonding. *Liq. Cryst.* **1999**, *26*, 965−971.
(38) Rinaldi, R.; Branca, E.; Cingolani, R.; Masiero, S.; Spada, G. P.; Gottarelli, G. Photodetectors fabricated from a self-assembly of a deoxyguanosine derivative. *Appl. Phys. Lett.* **2001**, *78*, 3541−3543.
(39) Rinaldi, R.; Maruccio, G.; Biasco, A.; Arima, V.; Cingolani, R.; Giorgi, T.; Masiero, S.; Spada, G. P.; Gottarelli, G. Hybrid molecular electronic devices based on modified deoxyguanosines. *Nanotechnology* **2002**, *13*, 398.
(40) Maruccio, G.; Visconti, P.; Arima, V.; D'Amico, S.; Blasco, A.; D'Amone, E.; Cingolani, R.; Rinaldi, R.; Masiero, S.; Giorgi, T.; Gottarelli, G. Field effect transistor based on a modified DNA base. *Nano Lett.* **2003**, *3*, 479−483.
(41) Liddar, H.; Li, J.; Neogi, A.; Neogi, P. B.; Sarkar, A.; Cho, S.; Morkoc, H. Self-assembled deoxyguanosine based molecular electronic device on GaN substrates. *Appl. Phys. Lett.* **2008**, *92*, 013309.
(42) Araki, K.; Takasawa, R.; Yoshikawa, I. Design, fabrication, and properties of macroscalesupramolecular fibers consisted of fully hydrogen-bonded pseudo-polymerchains. *Chem. Commun.* **2001**, 1826−1827.
(43) Sato, T.; Seko, M.; Takasawa, R.; Yoshikawa, I.; Araki, K. Mesoscopic-scale sheet-like assembly: critical role of inter-tape hydrogen bonds in the organogel formation and gel−liquid crystal transition of an alkylsilylated deoxyguanosine−dodecane system. *J. Mater. Chem.* **2001**, *11*, 3018−3022.
(44) Falk, M. Hydration of Purines, Pyramidines, Nucleosides and Nucleotides. *Can. J. Chem.* **1965**, *43*, 314−318.
(45) Falk, M. A Gravimetric Study of Hydration of Polynucleotides. *Can. J. Chem.* **1966**, *44*, 1107−1111.
(46) Sugawara, Y.; Iimura, Y.; Iwasaki, H.; Urabe, H.; Saito, H. Reversible Crystal Transition of Guanosine between the Dihydrate and Anhydrous States Coupled with Adsorption-Desorption Process. *J. Biomol. Struct. Dyn.* **1994**, *11*, 721−729.
(47) Yoneda, S.; Sugawara, Y.; Urabe, H. Crystal Water Dynamics of Guanosine Dihydrate: Analysis of Atomic Displacement Parameters, Time Profile of Hydrogen-Bonding Probability, and Translocation of Water by MD Simulation. *J. Phys. Chem. B* **2005**, *109*, 1304−1312.
(48) Brown, S. P. Probing proton-proton proximities in the solid state. *Prog. Nucl. Magn. Reson. Spectrosc.* **2007**, *50*, 199−251.
(49) Brown, S. P. Recent Advances in Solid-State MAS NMR Methodology for Probing Structure and Dynamics in Polymeric and Supramolecular Systems. *Macromol. Rapid Commun.* **2009**, *30*, 688−716.
(50) Oas, T. G.; Griffin, R. G.; Levitt, M. H. Rotary resonance recoupling of dipolar interactions in solid-state nuclear magnetic resonance spectroscopy. *J. Chem. Phys.* **1988**, *89*, 692−695.
(51) Cavadini, S.; Antonijevic, S.; Lupulescu, A.; Bodenhausen, G. Indirect detection of nitrogen-14 in solids via protons by nuclear magnetic resonance spectroscopy. *J. Magn. Reson.* **2006**, *182*, 168−172.
(52) Cavadini, S. Indirect detection of nitrogen-14 in solid-state NMR spectroscopy. *Prog. Nucl. Magn. Reson. Spectrosc.* **2010**, *56*, 46−77.
(53) Gan, Z. H.; Amoureux, J. P.; Trebosc, J. Proton-detected ^{14}N MAS NMR using homonuclear decoupled rotary resonance. *Chem. Phys. Lett.* **2007**, *435*, 163−169.
(54) Nishiyama, Y.; Endo, Y.; Nemoto, T.; Utsumi, H.; Yamauchi, K.; Hioka, K.; Asakura, T. Very fast magic angle spinning ^{1}H-^{14}N 2D solid-state NMR: Sub-micro-liter sample data collection in a few minutes. *J. Magn. Reson.* **2011**, *208*, 44−48.
(55) Tatton, A. S.; Bradley, J. P.; Iuga, D.; Brown, S. P. ^{14}N-^{1}H Heteronuclear Multiple-Quantum Correlation Magic-Angle Spinning NMR Spectroscopy of Organic Solids. *Z. Phys. Chem.* **2012**, *226*, 1187−1203.
(56) Tatton, A. S.; Pham, T. N.; Vogt, F. G.; Iuga, D.; Edwards, A. J.; Brown, S. P. Probing Hydrogen Bonding in Cocrystals and Amorphous Dispersions Using ^{14}N−^{1}H HMQC Solid-State NMR. *Mol. Pharmaceutics* **2013**, *10*, 999−1007.
(57) Webber, A. L.; Emsley, L.; Claramunt, R. M.; Brown, S. P. NMR Crystallography of Campho 2,3-c pyrazole (Z′ = 6): Combining High-Resolution ^{1}H-^{13}C Solid-State MAS NMR Spectroscopy and GIPAW Chemical-Shift Calculations. *J. Phys. Chem. A* **2010**, *114*, 10435−10442.
(58) Xu, J.; Terskikh, V. V.; Chu, Y.; Zheng, A.; Huang, Y. Mapping Out Chemically Similar, Crystallographically Nonequivalent Hydrogen Sites in Metal−Organic Frameworks by ^{1}H Solid-State NMR Spectroscopy. *Chem. Mater.* **2015**, *27*, 3306−3316.
(59) Khitrin, A.; Fung, B. M. Design of heteronuclear decoupling sequences for solids. *J. Chem. Phys.* **2000**, *112*, 2392.
(60) Elena, B.; Lesage, A.; Steuernagel, S.; Bockmann, A.; Emsley, L. Proton to Carbon-13 INEPT in Solid-State NMR Spectroscopy. *J. Am. Chem. Soc.* **2005**, *127*, 17296−17302.
(61) Elena, B.; de Paepe, G.; Emsley, L. Direct spectral optimization of proton−proton homonuclear dipolar decoupling in solid-state NMR. *Chem. Phys. Lett.* **2004**, *398*, 532−538.
(62) Schnell, I.; Lupulescu, A.; Hafner, S.; Demco, D. E.; Spiess, H. W. Resolution Enhancement in Multiple-Quantum MAS NMR Spectroscopy. *J. Magn. Reson.* **1998**, *133*, 61−69.
(63) Sommer, W.; Gottwald, J.; Demco, D. E.; Spiess, H. W. Dipolar Heteronuclear Multiple-Quantum NMR Spectroscopy in Rotating Solids. *J. Magn. Reson., Ser. A* **1995**, *113*, 131−134.
(64) Morcombe, C. R.; Zilm, K. W. Chemical shift referencing in MAS solid state NMR. *J. Magn. Reson.* **2003**, *162*, 479−486.
(65) Hayashi, S.; Hayamizu, K. Chemical shift standards in high-resolution solid-state NMR (1) ^{13}C, ^{29}Si, and ^{1}H nuclei. *Bull. Chem. Soc. Jpn.* **1991**, *64*, 685−687.
(66) Martin, G. E.; Hadden, C. E. Long-range ^{1}H-^{15}N heteronuclear shift correlation at natural abundance. *J. Nat. Prod.* **2000**, *63*, 543−585.
(67) Pickard, C. J.; Mauri, F. All-electron magnetic response with pseudopotentials: NMR chemical shifts. *Phys. Rev. B: Condens. Matter Mater. Phys.* **2001**, *63*, 245101.
(68) Yates, J. R.; Pickard, C. J.; Mauri, F. Calculation of NMR chemical shifts for extended systems using ultrasoft pseudopotentials. *Phys. Rev. B: Condens. Matter Mater. Phys.* **2007**, *76*, 024401.
(69) Clark, S. J.; Segall, M. D.; Pickard, C. J.; Hasnip, P. J.; Probert, M. J.; Refson, K.; Payne, M. C. First priciples methods using CASTEP. *Z. Kristallogr. - Cryst. Mater.* **2005**, *220*, 567−570.
(70) Perdew, J. P.; Burke, K.; Ernzerhof, M. Generalized Gradient Approximation Made Simple. *Phys. Rev. Lett.* **1996**, *77*, 3865.
(71) Tkatchenko, A.; Scheffler, M. Accurate Molecular Van Der Waals Interactions from Ground-State Electron Density and Free-Atom Reference Data. *Phys. Rev. Lett.* **2009**, *102*, 073005.
(72) Vanderbilt, D. Soft self-consistent pseudopotentials in a generalized eigenvalue formalism. *Phys. Rev. B: Condens. Matter Mater. Phys.* **1990**, *41*, 7892.
(73) http://www.ccpnc.ac.uk/magresview/.

DOI: 10.1021/acs.cgd.5b01440
Cryst. Growth Des. 2015, 15, 5945−5954